Inertial focusing of a neutrally buoyant particle in stratified flows

Cite as: Phys. Fluids **31**, 102006 (2019); https://doi.org/10.1063/1.5111419
Submitted: 30 May 2019 . Accepted: 08 August 2019 . Published Online: 16 October 2019

S. Kiran Jyothi, T. Renganathan, and S. Pushpavanam

Physics of Fluids ARTICLE scitation.org/journal/phf

Inertial focusing of a neutrally buoyant particle in stratified flows

Cite as: Phys. Fluids 31, 102006 (2019); doi: 10.1063/1.5111419
Submitted: 30 May 2019 • Accepted: 8 August 2019 •
Published Online: 16 October 2019

S. Kiran Jyothi, T. Renganathan, and S. Pushpavanam[a)]

AFFILIATIONS

Department of Chemical Engineering, IIT Madras, Chennai 600036, India

[a)]Author to whom correspondence should be addressed: spush@iitm.ac.in

ABSTRACT

Particles in microfluidic channels experience two dominant lift forces in the direction transverse to the flow—the shear gradient lift force and the wall lift force. These forces contribute to the lift experienced by the particle and cause their cross stream migration until they attain an equilibrium position where the net lift force in the transverse direction is zero. Stratified coflow of two liquids with different viscosities is a stable flow-regime observed under some operating conditions. The presence of the second fluid alters the shear gradient induced lift force and the wall force acting on the particle at each point, changing the final equilibrium position. These positions can be tuned and controlled by altering the viscosity or the flow rates of the two fluids so that the particles focus in one fluid. A numerical method based on the combined Immersed Boundary-Lattice Boltzmann Method is used to study inertial focusing of neutrally buoyant particles in stratified Couette flows and pressure driven flows. We analyze how different factors such as the Reynolds number, flow rate ratio, viscosity ratio of the fluids, and particle size affect the particle migration in two-dimensional (2D) and three-dimensional (3D) geometries. Our study shows that in Couette flows, the particle focuses in the low viscosity fluid when the interface is at the center. We also found that a critical viscosity ratio exists beyond which particle focusing in low viscous fluid is guaranteed, for a given flow rate ratio in pressure driven flows.

I. INTRODUCTION

Inertial focusing has emerged as a novel method to manipulate particles in microchannels. When a random distribution of particles enters and flows through a channel, they can migrate across streamlines and focus at certain fixed positions. This is induced by the inertial forces that act on the particle in the fluid and is called inertial focusing. It was first experimentally observed by Segré and Silberberg[1] in their experiments in circular pipes. They found that the particles focused at a radial position, which was 0.6 times the pipe radius from the center. Similar experiments using square and rectangular channels have revealed unique focusing positions across the cross sections.[2]

There are primarily two forces that control the focusing positions in channels. The first is the shear gradient lift force, which arises due to the asymmetry in the relative velocity between the fluid and the particle on either side of the particle. This asymmetry occurs when the velocity profile is curved as in a pressure driven flow. The shear gradient lift force acts in the direction that can reduce the asymmetry in the relative velocity, which in most cases is toward the wall. The other prominent force that acts on the particle is a wall repulsion force, which is due to a pressure increase between the particle and the wall, causing the particle to move away from the wall.[2] At the focusing positions, which we observe experimentally, these two forces nullify each other. Inertial focusing can be exploited to develop applications in diverse fields such as membrane free filtration[3] and separation of cells.[4]

Earlier works have investigated the effects of factors such as the Reynolds number and particle size on the focusing position. Di Carlo *et al.*[5] showed that for a comparatively larger particle size to width ratio of 0.22, particles equilibrate along the axes for the Reynolds numbers in the range of 20–80 for a square channel. This was in contrast to the work of Prohm and Stark[6] who showed that particles equilibrate along the diagonals for Reynolds number ranges of 10–80. This contradiction may be attributed to the difference in particle sizes studied or the sensitivity of the system to operating conditions. For a higher range of Reynolds numbers, Miura *et al.*[7] and Nakagawa *et al.*[8] showed that there exists a critical Reynolds number

for a system beyond which a transition from axially stable positions to diagonally stable positions occurs. Chun and Ladd[9] have confirmed the existence of stable diagonal equilibrium positions at very high Reynolds numbers through their simulations. Bhagat *et al.*[10] have shown that particles equilibrate along the longer dimension for rectangular channels. These studies on single phase flows show that the equilibrium positions can be changed by controlling the Reynolds number and particle size.

Particle focusing in single phase systems has also been studied numerically extensively. Feng *et al.*[11] used finite element analysis to study the motion of particles in shear flows and pressure driven flows, and Di Carlo *et al.*[5] studied particle motion in a three dimensional square channel using the same framework. Shamloo and Mashhadian[12] also used finite element analysis to study the effect of angular velocity, particle density, and particle diameter on the focusing behavior in serpentine channels on a centrifugal platform. Inamuro *et al.*[13] studied the motion of a line of neutrally buoyant circular cylinders using a stress tensor integration method to compute the forces acting on the particle arising from the fluid-particle interaction, using an LBM (Lattice Boltzmann Method) simulation. Verberg and Ladd[14] used LBM to simulate particle laden flows using a bounce back rule at the particle boundary to enforce no-slip. They approximated the particle surface using a stairway approximation and later extended it for higher Reynolds numbers.[9] LBM coupled with the bounce back rule was also used recently to study the effect of the particle concentration and Reynolds number by Liu and Wu.[15] Hu and Guo[16] investigated the motion of a neutrally buoyant particle taking into consideration thermal effects, using an iterative predictive and correction approach around the particle boundary using LBM. To couple the particle motion with fluid dynamics, IBM (Immersed Boundary Method) has been popularly used in conjunction with LBM.[17–19] IBM allows us to represent particles of arbitrary shape without any approximation. The elegant coupling between the LBM and IBM and the ease of parallelization of LBM have made the IB-LBM (Immersed Boundary-Lattice Boltzmann Method) a popular technique for solving particle laden flows.

For a given geometry and operating conditions, the focusing positions are fixed for single phase flows. Changing the shape of the velocity profile in a channel alters the forces acting on the particles and allows us to tune the equilibrium position of the particles. One way to achieve this is to introduce stratified flow in a channel. Here, two fluids flow alongside each other and the symmetric parabolic Hagen-Poiseuille flow profile gets modified. The velocity profile is determined by the viscosity of the two fluids involved and their flow rates. Hence, when the geometry of the system is fixed, the viscosity ratio and the flow rates of the two liquids in stratified flow allow us an extra degree of freedom to control the focusing positions. In the Couette flow, the velocity profile is linear and hence shear gradient is absent. But the introduction of viscosity stratification can alter the centerline focusing positions exhibited in single phase flows. In stratified pressure driven flows, the flow rates of the two liquids influence the focusing behavior along with the viscosity ratio of the two liquids. Lee *et al.*[20] in their experimental work have demonstrated interfacial focusing behavior for high viscosity ratios of fluids and low particle sizes. Gossett *et al.*[21] have shown experimentally the tendency of particles to migrate from one fluid to another depending on operating conditions. The transfer of particles occurs only when all the stable equilibrium positions of the system lie in the receiving fluid. The motivation for this work is to quantitatively understand the role of parameters such as the viscosity ratio, the flow-rate ratio, and the Reynolds number in controlling the equilibrium positions. This will help design point of care diagnostic systems and membrane-less filtration systems whose operations are based on transfer of particles or cells from one fluid to another. A specific application of this is in removing particles or cells from a fluid without using a membrane. Eliminating a membrane in the process helps overcome the problem of fouling and lowers the hydrodynamic resistance in the system. Particle focusing in stratified flows has not been investigated theoretically. This motivates us to numerically analyze the effect of the abovementioned factors in a stratified flow system.

As a first step in this work, we neglect the effects of interfacial tension and represent the system as a single-phase system with a sharp viscosity stratification. The system has two different viscosity values on either side of a predefined interface. The particle is assumed to be neutrally buoyant. The densities of the two fluids are assumed to be equal. For the current study, we limit the range of the Reynolds number to the order of 10 as this is the range in which microfluidic separation devices operate. The lattice Boltzmann method is adopted to determine the flow field as it is ideally suited for the length scales associated with microfluidics.[22] It may be unstable at very high Reynolds numbers or for low viscosity fluid flows, but it is suitable for the low Reynolds number regime we consider for our simulations. This is coupled with the immersed boundary method to numerically simulate particle fluid interaction in the two flow systems.

The paper is organized as follows. Section II describes the algorithm and the numerical methods used for simulations. Section III details the geometry of the systems analyzed in this work. Section IV explains the validations done for the code developed using results from previous studies. Section V contains the results obtained from the simulations carried out for stratified Couette and pressure driven flows. Here, both two-dimensional (2D) and three-dimensional (3D) flows are simulated. Section VI summarizes the main results.

II. NUMERICAL METHOD ADOPTED

A. IB-LBM

The fluid flow is described using the equation of continuity and the Navier Stokes equation as given in the following set of equations:

$$\nabla \cdot \boldsymbol{u} = 0, \tag{1}$$

$$\rho\left(\frac{\partial \boldsymbol{u}}{\partial t} + \boldsymbol{u} \cdot \nabla \boldsymbol{u}\right) = -\nabla p + \mu \nabla^2 \boldsymbol{u} + \boldsymbol{f}. \tag{2}$$

Here, all variables have standard significance and $\boldsymbol{f}$ describes the external forces acting in the fluid, which would be described in Sec. II B. These equations are solved using the lattice Boltzmann method, while the immersed boundary method couples the fluid and particle dynamics. In IBM, we assume the particle surface to be a membrane with a finite density, filled with liquid inside it. The particle boundary is represented using a set of N Lagrangian points, which do not necessarily lie on the Eulerian grids in which the fluid

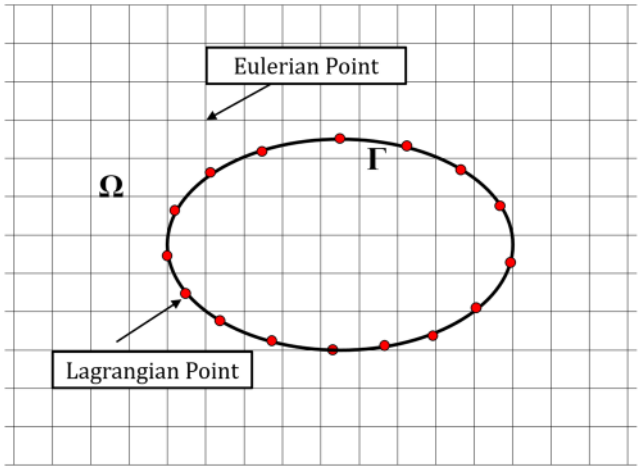

FIG. 1. Illustration of particle in fluid domain. The fluid flow is solved at the Eulerian grid points, while the forces and velocities on the particle surface are determined at the Lagrangian points.

variables are solved. The particle boundary Γ lies in the fluid domain Ω, as shown in Fig. 1.

The fluid velocity values at the Lagrangian points are unknown to begin with. These are obtained by interpolation from the known velocities at the Eulerian points using

$$\boldsymbol{U}(s,t) = \int_{\Omega} \boldsymbol{u}(\boldsymbol{x},t)\delta(\boldsymbol{x} - \boldsymbol{X}(s,t))d\boldsymbol{x}, \tag{3}$$

where $\boldsymbol{U}(s,t)$ represents the Lagrangian velocity, $\boldsymbol{u}(\boldsymbol{x},t)$ represents the Eulerian velocity, and δ is the Dirac-delta function. The interpolated fluid velocity is not necessarily equal to the particle velocity. The no-slip boundary condition requires the fluid and particle velocities to be equal at the Lagrangian points. To ensure this, we assume the particle exerts external correction forces $\boldsymbol{F}^{corr}(s,t)$ at the boundary. These forces are then distributed on to the Eulerian nodes using the formula

$$\boldsymbol{f}^{corr}(\boldsymbol{x},t) = \int_{\Gamma} \boldsymbol{F}^{corr}(s,t)\delta(\boldsymbol{x} - \boldsymbol{X}(s,t))ds. \tag{4}$$

The velocity of the fluid is then modified using these forces. The discretized forms of Eqs. (3) and (4) are used in the IB-LBM formulation. We next describe the lattice Boltzmann method and the numerical algorithm adopted in this work.

B. Lattice Boltzmann method

The lattice Boltzmann method uses a discretized version of the Boltzmann equation, which describes the evolution of a particle density function $f(\boldsymbol{x},\boldsymbol{c},t)$ at position $\boldsymbol{x}$ with velocity $\boldsymbol{c}$ at time t. In the discretized form, we consider a restricted set of velocity vectors. The set of velocity vectors are defined by the model chosen, which is represented as DdQq, where d represents the dimensionality of the system and q represents the number of discrete velocity vectors. As the number of velocity vectors considered increases, the accuracy of the solution increases, but this is at a higher cost of computation.

For this work, we define 2D domains using the D2Q9 model and 3D domains using the D3Q19 model. Since we consider only the laminar flow regime for our discussions, these velocity sets are sufficient to capture the relevant physical phenomena in a computationally efficient way. The D2Q9 model is represented using the velocity vectors $\boldsymbol{c_i}$ = (0, 0), (±1, 0), (0, ±1), and (±1, ±1) for i = 0, 1, 2, . . ., 9, and the D3Q19 model is represented by the velocity vectors $\boldsymbol{c_i}$ = (0, 0, 0), (±1, 0, 0), (0, ±1, 0), (0, 0, ±1), (±1, ±1, 0), (±1, 0, ±1), and (0, ±1, ±1) for i = 0, 1, 2, . . ., 19.

Here, $f_i(\boldsymbol{x},t)$ represents the density distribution function of a particle at $\boldsymbol{x}$ moving with velocity $\boldsymbol{c_i}$ at time t. The discretized lattice Boltzmann equation is then represented as

$$f_i(\boldsymbol{x} + \boldsymbol{c_i}\Delta t, t + \Delta t) = f_i(\boldsymbol{x},t) - \frac{\Delta t}{\tau}\left(f_i(\boldsymbol{x},t) - f_i^{eq}(\boldsymbol{x},t)\right), \tag{5}$$

where τ is the relaxation time, which determines the rate of approach to the equilibrium distribution f_i^{eq}. The equilibrium distribution function f_i^{eq} is given by

$$f_i^{eq}(\boldsymbol{x},t) = w_i\rho\left(1 + \frac{\boldsymbol{u}\cdot\boldsymbol{c_i}}{c_s^2} + \frac{(\boldsymbol{u}\cdot\boldsymbol{c_i})^2}{2c_s^4} - \frac{\boldsymbol{u}\cdot\boldsymbol{u}}{2c_s^2}\right). \tag{6}$$

Here, ρ and **u** are the density and velocity values at position **x** and time t. w_i are weights defined as w_o = 4/9, $w_{1\text{-}4}$ = 1/9, and $w_{5\text{-}8}$ = 1/36 for the D2Q9 velocity set and w_o = 1/3, $w_{1\text{-}6}$ = 1/18, $w_{7\text{-}18}$ = 1/36 for the D3Q19 velocity set. c_s represents the speed of sound in lattice units and has a value $\frac{1}{\sqrt{3}}$.

A Chapman-Enskog analysis shows that the equation of continuity and the Navier-Stokes equations can be recovered from the lattice Boltzmann equation. The macroscopic variables ρ, **u** and the pressure (p) are obtained using

$$\rho(\boldsymbol{x},t) = \sum_i f_i(\boldsymbol{x},t), \tag{7}$$

$$\rho\boldsymbol{u}(\boldsymbol{x},t) = \sum_i f_i(\boldsymbol{x},t)\boldsymbol{c_i}, \tag{8}$$

$$p = \rho c_s^2. \tag{9}$$

The kinematic viscosity (ϑ) of the system is related to the relaxation time (τ) as

$$\vartheta = c_s^2\left(\tau - \frac{\Delta t}{2}\right). \tag{10}$$

As a first step to analyze the stratified flows, we neglect interfacial tension. This allows us to represent the stratified flow as a single phase system with two different viscosity values on either side of the interface. We change the relaxation time parameter (τ) on either side of a predefined interface location to incorporate this effect. Forces acting on the fluid are included in the lattice Boltzmann equation. Since we are using IBM coupled with LBM, correction forces acting on the fluid arise as explained in Sec. II A. The final form of the equation including these correction forces and any external force acting on the system is given by the following equation:

$$f_i(\boldsymbol{x} + \boldsymbol{c_i}\Delta t, t + \Delta t) = f_i(\boldsymbol{x},t) - \frac{\Delta t}{\tau}\left(f_i(\boldsymbol{x},t) - f_i^{eq}(\boldsymbol{x},t)\right) + F_i^{corr}(\boldsymbol{x},t)\Delta t + F_i^{ext}(\boldsymbol{x},t)\Delta t, \tag{11}$$

where F_i^{corr} and F_i^{ext} are the lattice force terms for the correction forces $\boldsymbol{f}^{corr}$ and external forces $\boldsymbol{f}^{ext}$ defined as

$$F_i^{corr} = w_i \frac{\boldsymbol{c_i} \cdot \boldsymbol{f}^{corr}}{c_s^2}, \tag{12}$$

$$F_i^{ext} = w_i \frac{\boldsymbol{c_i} \cdot \boldsymbol{f}^{ext}}{c_s^2}. \tag{13}$$

The lattice Boltzmann method is implemented in two steps: (a) collision step and (b) streaming step. During the collision step, the values obtained from the RHS of Eq. (5) are stored in an intermediate variable f_i^*,

$$f_i^*(\boldsymbol{x}, t) = f_i(\boldsymbol{x}, t) - \frac{\Delta t}{\tau}\left(f_i(\boldsymbol{x}, t) - f_i^{eq}(\boldsymbol{x}, t)\right). \tag{14}$$

The obtained variables are streamed, i.e., the values are then spread on to adjacent grids depending on the value of $\mathbf{c_i}$ using

$$f_i'(\boldsymbol{x} + \boldsymbol{c_i}\Delta t, t) = f_i^*(\boldsymbol{x}, t). \tag{15}$$

After the populations are streamed, the force terms are incorporated,

$$f_i(\boldsymbol{x}, t + \Delta t) = f_i'(\boldsymbol{x}, t) + F_i^{corr}(\boldsymbol{x}, t)\Delta t + F_i^{ext}(\boldsymbol{x}, t)\Delta t. \tag{16}$$

The simulation parameters are chosen so that we recover the nondimensional parameters as described in Subsection 1 of the Appendix. The method also employs the bounce back approach and wet node approach to implement the no-slip boundary conditions, as described in Subsection 2 of the Appendix. Further details about the method can be found in the work of Krüger *et al.*[23]

C. Implicit velocity correction

There are several approaches available in the literature to implement IB-LBM. The differences lie in how the forces that ensure no-slip at the boundary are evaluated. Peskin[24] originally used a force correction method assuming the Lagrangian points as links that exert a spring type restoration force after the points are displaced by the interpolated velocity. Later, the direct forcing approach was introduced in which the force was proportional to the difference between the interpolated velocity and the actual particle velocity. However, these methods do not always satisfy the no slip condition at the particle boundary. Later, the direct forcing method was modified as the multidirect forcing method.[19] An implicit force correction method was developed,[18] which determines the force values exactly. We adopt this method as it is more accurate and computationally faster.

In this method, the fluid velocity is modified using an initially unknown correction $\delta\boldsymbol{u}$ as

$$\boldsymbol{u} = \boldsymbol{u}^* + \delta\boldsymbol{u}. \tag{17}$$

Here, $\boldsymbol{u}^*$ is the velocity obtained using Eq. (8) from the particle density functions after adding the F_i^{ext} term but prior to adding the F_i^{corr} term. The velocity correction at the Eulerian points is interpolated from the velocity corrections at the Lagrangian points $\delta\mathbf{U}$ using an expression analogous to Eq. (4). These corrections are found using the following discrete form:

$$\delta\boldsymbol{u}(\boldsymbol{x}, t) = \sum_k \delta\boldsymbol{U}(\boldsymbol{X_k}, t) W(\boldsymbol{x} - \boldsymbol{X_k})\Delta s. \tag{18}$$

Here, $\boldsymbol{x}$ and $\boldsymbol{X_k}$ represent the Eulerian grid point and kth Lagrangian point, respectively, and Δs is the arclength between two Lagrangian points. W(**r**) is a discretized form of the Dirac delta function[25] defined as

$$W(\boldsymbol{r}) = \frac{1}{\Delta x \Delta y \Delta z} w\left(\frac{x}{\Delta x}\right) w\left(\frac{y}{\Delta y}\right) w\left(\frac{z}{\Delta z}\right), \quad w(r) = \begin{cases} 1 - |r|, & |r| \le 1 \\ 0, & |r| > 1 \end{cases}. \tag{19}$$

The forces acting on the fluid are related to these corrections as

$$\boldsymbol{f}^{corr} = \rho \frac{\delta\boldsymbol{u}}{\delta t}. \tag{20}$$

To satisfy the no slip condition, the interpolated velocity after correction must be set equal to the particle velocity at its boundary ($\mathbf{U_k}$), so

$$\boldsymbol{U_k}(\boldsymbol{X_k}, t) = \sum_x \boldsymbol{u}(\boldsymbol{x}, t) W(\boldsymbol{x} - \boldsymbol{X_k})(\Delta x)^d. \tag{21}$$

Here, d represents the dimensionality of the system. From Eqs. (17) and (18), we obtain

$$\boldsymbol{U_k}(\boldsymbol{X_k}, t) = \sum_x \boldsymbol{u}^*(\boldsymbol{x}, t) W(\boldsymbol{x} - \boldsymbol{X_k})(\Delta x)^d + \sum_x \sum_l \delta\boldsymbol{U}(\boldsymbol{X_k}, t) \times W(\boldsymbol{x} - \boldsymbol{X_k})(\Delta s) W(\boldsymbol{x} - \boldsymbol{X_l})(\Delta x)^d. \tag{22}$$

Equation (22) is rearranged as a linear system of equations,

$$\begin{aligned} Ay &= b, \\ A_{kl} &= \sum_x W(\boldsymbol{x} - \boldsymbol{X_k})(\Delta s) W(\boldsymbol{x} - \boldsymbol{X_l})(\Delta x)^d, \\ y_k &= \delta\boldsymbol{U}(\boldsymbol{X_k}, t), \\ b_k &= \boldsymbol{U_k}(X_k, t) - \sum_x \boldsymbol{u}^*(\boldsymbol{x}, t) W(\boldsymbol{x} - \boldsymbol{X_k})(\Delta x)^d. \end{aligned} \tag{23}$$

A is a N × N matrix and y and b are N × 1 vectors. We first determine $\delta\mathbf{U}$ using the above system of equations. We then find the corresponding velocity corrections $\delta\boldsymbol{u}$ and force values $\boldsymbol{f}^{corr}$ at the Eulerian points from Eqs. (18) and (20), respectively. These force terms are then added to the LB equation to correct the f_i values as per Eq. (16). The macroscopic variables are recomputed using Eqs. (7)–(9).

D. Determination of focusing positions

Two methods can be employed to determine the focusing positions. The first involves tracking the particle dynamically by considering the particle motion. The second involves computing a lift force plot. We now describe both the methods in detail.

1. Particle motion

We have discussed how the force on the fluid is determined. The particle is acted upon by the negative of the forces exerted on to the fluid. We use Newton's equations of translational and rotational motion of particle to describe its motion,

$$M_B \frac{d\boldsymbol{U_B}}{dt} = \oint_{\partial s} \tilde{\boldsymbol{\sigma}} \cdot \boldsymbol{n} ds + \left(\rho_B - \rho_f\right) V_B \boldsymbol{g}, \tag{24}$$

$$I_B \frac{d\boldsymbol{\omega_B}}{dt} = \oint_{\partial s} (\boldsymbol{X_k} - \boldsymbol{X_B}) \times (\tilde{\boldsymbol{\sigma}}.\boldsymbol{n}) ds, \tag{25}$$

$$\boldsymbol{U_k} = \boldsymbol{U_B} + \boldsymbol{\omega_B} \times (\boldsymbol{X_k} - \boldsymbol{X_B}). \tag{26}$$

Here, M_B and I_B are the mass and moment of inertia of the particle. $\boldsymbol{U_B}$ and $\boldsymbol{\omega_B}$ are the translational and angular velocities of the center of mass of the particle. $\tilde{\boldsymbol{\sigma}}$ is the fluid stress tensor and $\boldsymbol{n}$ indicates the direction of the outward normal from the surface of the particle. ρ_B and ρ_f are the density values of the particle and the fluid, respectively. V_B and $\boldsymbol{X_B}$ are the volume of the particle and the position of the particle center. The external force acting on the particle (gravity) is incorporated in the $\boldsymbol{g}$ term. Following Feng and Michaelides,[26] the equations of motion are discretized as

$$\boldsymbol{U_B^{n+1}} = \left(1 + \frac{\rho_f}{\rho_B}\right)\boldsymbol{U_B^n} - \frac{\rho_f}{\rho_B}\boldsymbol{U_B^{n-1}} + \frac{(-\sum_k \boldsymbol{F_k}^{corr}\delta V)\delta t}{M_B} + \left(1 - \frac{\rho_f}{\rho_B}\right)\boldsymbol{g}\delta t, \tag{27}$$

$$\boldsymbol{\omega_B^{n+1}} = \left(1 + \frac{\rho_f}{\rho_B}\right)\boldsymbol{\omega_B^n} - \frac{\rho_f}{\rho_B}\boldsymbol{\omega_B^{n-1}} + \boldsymbol{I_B}^{-1}\sum_{\boldsymbol{k}}(\boldsymbol{X_k} - \boldsymbol{X_B}) \times (-\boldsymbol{F_k}^{corr})\delta V, \tag{28}$$

where superscript "n" represents the n-th time instant value. The particle position is then updated using

$$\boldsymbol{X_B^{n+1}} = \boldsymbol{X_B^n} + \boldsymbol{U_B^{n+1}}\Delta t. \tag{29}$$

Following these steps gives us the trajectory of the particle over a period of time. The positions of the particle at steady state in the lateral direction would give us the equilibrium positions of the given system.

2. Lift force curve

An alternate method to find the equilibrium positions is to construct a lift-force curve that gives the lift force acting on the particle at different positions along the lateral direction. The points where the force is zero denote the equilibrium positions for the given system. To construct the lift-force curve, the simulation is conducted by restricting the movement of the particle in the lateral direction. The force acting on the particle in the lateral direction is found once the simulation converges. This procedure is repeated for different positions along the lateral direction to obtain the complete lift force curve.

E. Algorithm

To summarize, the algorithm to determine the focusing positions consists of the following steps:

1. Initialize the density distribution function $f_i(\boldsymbol{x}, t)$ and the particle variables $\boldsymbol{X_B}$, $\boldsymbol{U_B}$, and $\boldsymbol{\omega_B}$.
2. Update the translational and angular velocities of the center of mass of the particle, $\boldsymbol{U_B}$ and $\boldsymbol{\omega_B}$, using Eqs. (27) and (28).
3. Update the position of the center of the particle, $\boldsymbol{X_B}$, using Eq. (29). The positions of the Lagrangian points are updated accordingly.
4. Find the particle velocity at the Lagrangian points using Eq. (26).
5. Carry out the collision (14) and streaming (15) steps to find $f_i'(\boldsymbol{x}, t)$. The external force term is added to $f_i'(\boldsymbol{x}, t)$ as per Eq. (16).
6. Find the intermediate velocities prior to correction, $\boldsymbol{u}^*$, using Eq. (8).
7. Solve the system of linear equations (23) to obtain the Lagrangian velocity corrections, $\delta\boldsymbol{U}$.
8. Find the Eulerian velocity corrections, $\delta\boldsymbol{u}$, by interpolating $\delta\boldsymbol{U}$ using (18). Find the corresponding correction forces $\boldsymbol{f}^{corr}$ at the Eulerian points using Eq. (20).
9. Correct the $f_i'(\boldsymbol{x}, t)$ values, as per Eq. (16) using the correction forces determined.
10. Find the macroscopic fluid density and velocities using Eqs. (7) and (8).
11. Find the new equilibrium function, $f_i^{eq}(\boldsymbol{x}, t)$, using Eq. (6).
12. Go back to step 2 and iterate until convergence.

To find the lift force curve, the particle motion in the lateral direction is not performed. When the simulation converges, the total lateral force is determined. This is then carried out for different positions in the lateral direction. The simulations are performed using a MATLAB code run on a 3.6 GHz CPU (Intel Core i7-6700) with 32 GB RAM. The evaluation of the lift force for each operating condition took approximately 15 h.

III. SIMULATION MODEL

In this work, inertial focusing in Couette flows and pressure driven flows is analyzed. A schematic of the system of a particle in a Couette flow is represented in Fig. 2. The height of the channel was specified as H lattice units, while the diameter of the particle was specified as a lattice units. The shear was introduced by moving the top wall with a velocity U_w, while the bottom wall was kept stationary. Wet node boundary conditions were used on the walls[23] to impose no slip. L lattice units were used along the axial (flow)

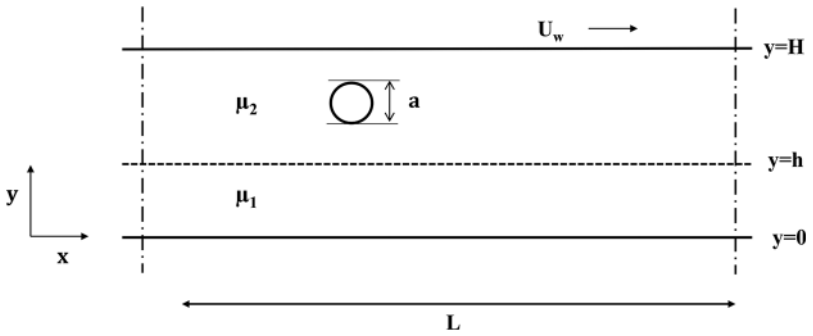

FIG. 2. Schematic of the system being studied for particle focusing in a 2D Couette flow.

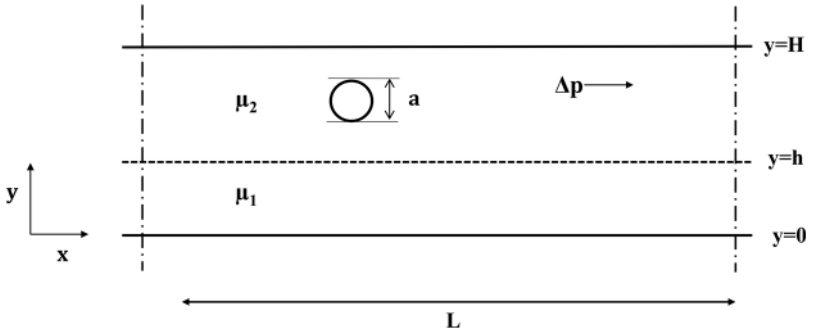

FIG. 3. Schematic of the system being studied for particle focusing in a 2D pressure driven flow.

direction. To simulate an infinitely long channel, periodic conditions were imposed in that direction. The interface position where the two liquids are in contact was defined explicitly as h, and two different relaxation time constants were specified on either side of the interface to incorporate the difference in viscosity (μ) of the two fluids. The parameters related to the top fluid were described using subscript 2 and those related to the bottom fluid were described using subscript 1. The Reynolds number (Re) of the system was described as $Re = \frac{U_w H}{\vartheta_2}$, where ϑ_2 is the kinematic viscosity of the upper fluid.

Figure 3 depicts the geometry of the system for 2D pressure driven flows. Here, both the walls were kept stationary. For 3D simulations, a third dimension extending to W lattice units perpendicular to the plane of the paper was introduced. A constant force density was applied throughout the domain in the axial direction to represent the pressure drop. The Reynolds number is defined as $Re = \frac{q_2}{\vartheta_2}$, where q_2 is the flow rate per unit width of the top fluid for 2D systems, and as $Re = \frac{q_2}{H\vartheta_2}$ for 3D systems, where q_2 is the flow rate of the top fluid.

IV. VALIDATION OF CODE

A. Particle in a Couette flow

To validate the IB-LBM code developed, the 2D single phase Couette flow is simulated and our results are compared with those reported by Feng and Michaelides[17] who also used a similar IB-LBM approach. They used a constant velocity ($U_w/2$) on the top wall, while a velocity of ($-U_w/2$) was imposed on the bottom wall. The parameters in lattice Boltzmann units used for the simulation are H = 80, τ = 0.6, a/H = 0.25, and U_w = 1/60. Since shear gradient is absent for this flow, the particle experiences only the symmetric counteracting wall forces from either side. Hence, the equilibrium position is at the centerline of the channel. The trajectory of a particle is traced and compared with the results reported by Feng and Michaelides[17] for Re = 40, a/H = 0.25. The two trajectories are found to be in good agreement, as seen in Fig. 4. The slight discrepancy observed is attributed to the finer grid used by Feng and Michaelides[17] in the axial direction, reducing particle-particle interaction arising due to the periodic boundary conditions.

B. Equivalence of the lift force curve and the trajectory of particle approaches

The final positions of the particle in its trajectories must correspond to the stable equilibrium positions in the lift force curve. Figure 5(a) shows the trajectories for a particle in a pressure driven single phase flow for different initial lateral positions obtained using our algorithm. The trajectories converge at two positions y = 0.29H and y = 0.71H depending on the initial position. Figure 5(b) is the lift force curve for the same system with the force normalized by $\rho U^2 a^2$, where U is the maximum undisturbed velocity. The lift force curve shows an unstable equilibrium position and two stable equilibrium positions on either side of it. The stable equilibrium position closer to the top wall is denoted as S2 and the position closer to the bottom wall is denoted as S1. For initial positions of the particle above the unstable equilibrium position and below S2, the particle is acted on by a net lift force in the positive y direction, and hence, it will focus at S2. Likewise, if the initial position of the particle lies below the unstable position and above S1, the particle is acted on by a net lift force in the negative y direction and is focused at S1. So, the final focusing position depends on the initial position of the particle. We were able to show that the stable positions obtained by the lift force curve are identical with the equilibrium positions obtained by the particle trajectories. Henceforth, we would be adopting the lift force curve approach to determine the stable equilibrium positions of the particle.

C. Particle in a pressure driven flow

The code developed for the 2D stratified flow is validated for a single phase pressure driven flow by using equal viscosity values

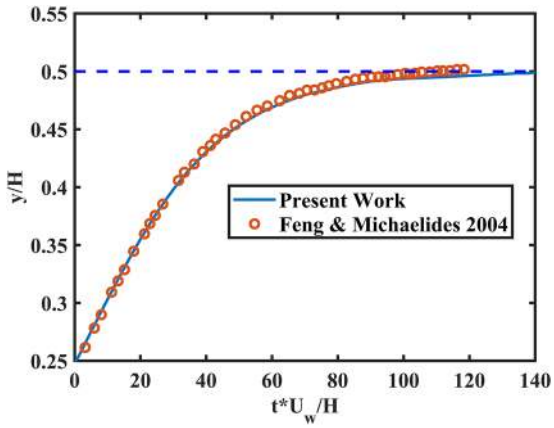

FIG. 4. Trajectory of a particle in a Couette flow over time (Re = 40, a/H = 0.25).

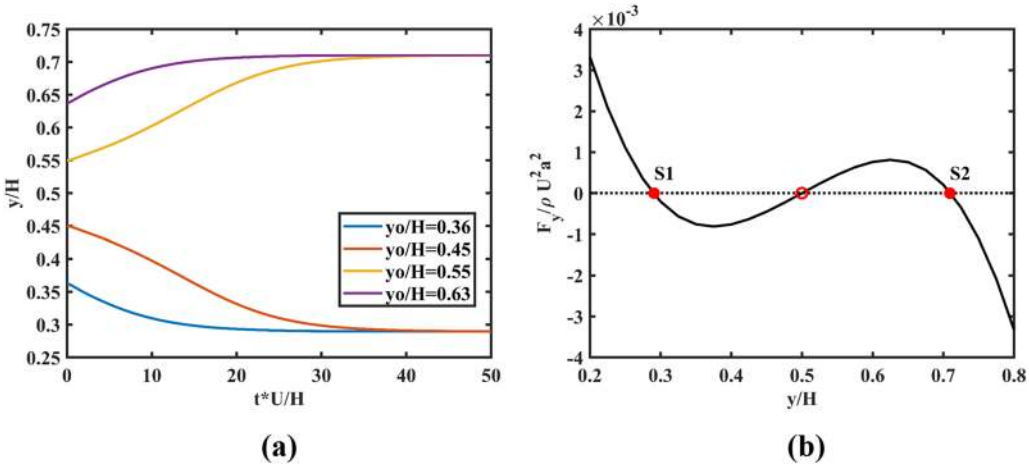

FIG. 5. (a) Trajectories of a particle in a pressure driven flow for different initial positions for Re = 40 and a/H = 0.25. (b) Lift force curve for the same system (red filled circle: stable equilibrium position; red hollow circle: unstable equilibrium position). The equilibrium positions obtained by the two methods are identical.

on either side of the interface. Inamuro *et al.*[13] performed similar simulations using the lattice Boltzmann method. Simulations were conducted keeping the Reynolds number and lattice parameters the same as in their work: L = 200, H = 200, τ = 0.757, a/H = 0.25, and Re = 191.48. The stable equilibrium positions predicted by the lift force curve for the given parameters (Fig. 6) are 0.27 and 0.73. The first point is in good agreement with the equilibrium position of 0.2706 reported by Inamuro *et al.*[13]

V. RESULTS AND DISCUSSION

Having validated the code developed for 2D flows with the literature, we now proceed to describe particle focusing in stratified flows.

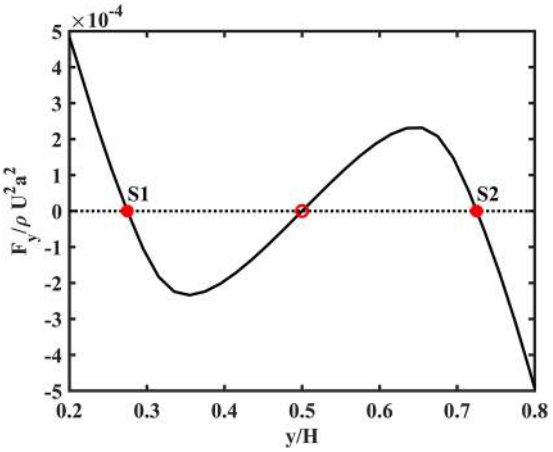

FIG. 6. Lift force curve for the particle in a pressure driven flow for Re = 191.48 and a/H = 0.25. (Red filled circle: stable equilibrium position; red hollow circle: unstable equilibrium position.)

A. 2D stratified Couette flow

We analyze the effect of different parameters such as the particle size, Reynolds number, and viscosity ratio on particle migration in a stratified Couette flow. The viscosity of the top fluid (ν_2) is fixed as 0.1 in lattice units, and the viscosity of the bottom fluid is varied to analyze the effect of different viscosity ratios. To find the equilibrium positions, the lift force curve is determined in each case. Figures 7(a) and 7(b) show the lift curves for two different viscosity ratios, 0.25 and 4. The lift force curve exhibits an extremum near the interface, which is caused by a change in the velocity gradient at the interface. The lift force in the less viscous fluid is similar to that seen in the single phase Couette flow. The position where the lift curve becomes zero gives us the equilibrium position.

1. Effect of viscosity ratio

Figure 8 shows the effect of the viscosity ratio on the focusing positions for a fixed Re and particle size when the interface is at the center of the channel. The equilibrium position is always at the center for a viscosity ratio of unity for all parameters, as it represents a single phase flow. The shift in the equilibrium positions for other viscosity ratios is caused by the asymmetry introduced in the system due to the viscosity stratification. This becomes more prominent as the viscosity ratio deviates more from unity. When the viscosity ratio is less than one, the focusing position lies in the top fluid, while it lies in the bottom fluid when the viscosity ratio is more than one. This indicates that in all cases, the particle focuses in the less viscous fluid when the interface is located midway between the plates.

2. Effect of interface position

We next analyze the effect of the interface position on the equilibrium position. This is shown in Fig. 9. For a given viscosity ratio, when the interface is closer to the moving wall, the equilibrium positions are found closer to the moving wall. If the interface position

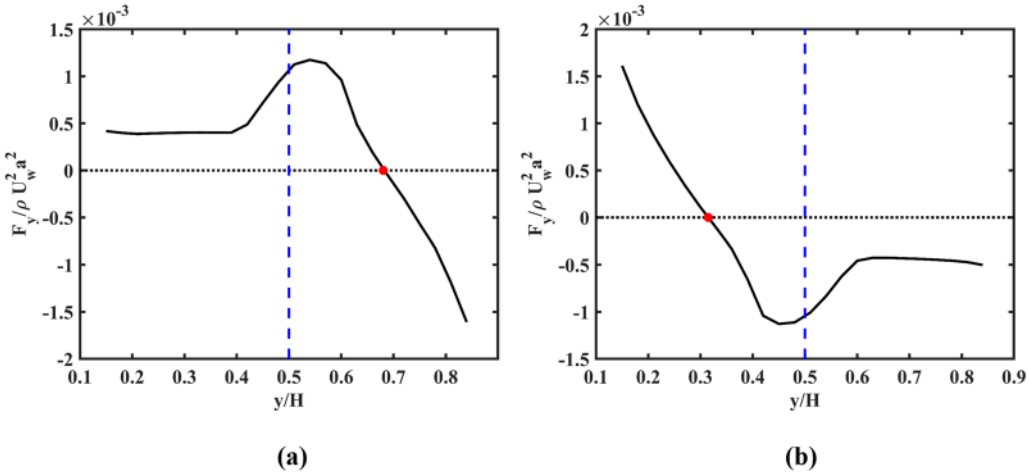

FIG. 7. Lift force curves for stratified flows (Re = 10, a/H = 0.2, h = 0.5). (a) μ_2/μ_1 = 0.25 and (b) μ_2/μ_1 = 4. The equilibrium positions obtained are 0.68 and 0.31, respectively. (Red circle: equilibrium position; blue dashed line: interface position).

moves away from the moving wall, the equilibrium positions also move away from the moving wall.

3. Effect of particle size

The effect of the particle size on the equilibrium positions in the shear flow is shown in Fig. 10. We observe that the smaller particle focuses closer to the nearer wall for any μ_2/μ_1. This result is also in line with what was reported by Gossett *et al.*[21] The analytical expression for the wall lift force is $F_{LW} \propto \frac{\rho U^2 a^6}{H^4}$.[2] This implies that the wall repulsion force is lower for a smaller particle, explaining why the smaller particle is focused closer to the wall.

4. Effect of Reynolds number

The Reynolds number did not have a significant effect on the focusing positions in the case of the stratified shear flow. In Fig. 11, we see that the equilibrium positions are almost independent of Re for each viscosity ratio. The equilibrium positions do not get affected even for a Reynolds number value of 100, as we can see from Table I. This is attributed to the fact that the velocity profile is piecewise linear, and hence, no shear gradient force exists in the system.

B. 2D stratified pressure driven flow

In a pressure driven stratified flow, the pressure gradient and the interface position uniquely determine the system for a particular

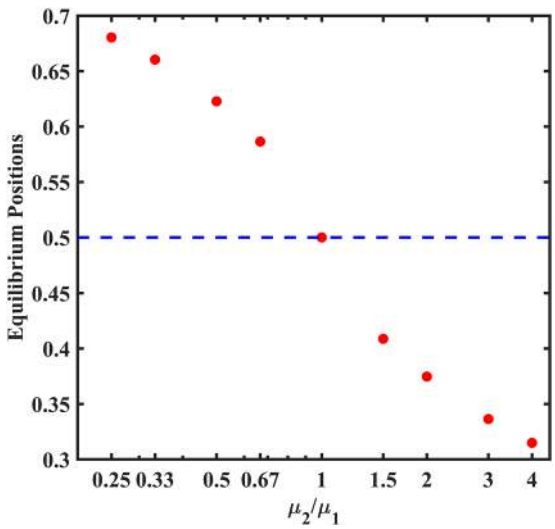

FIG. 8. Effect of the viscosity ratio on equilibrium positions (Re = 10, a/H = 0.2, and h = 0.5) (red circle: equilibrium positions; blue dashed line: interface).

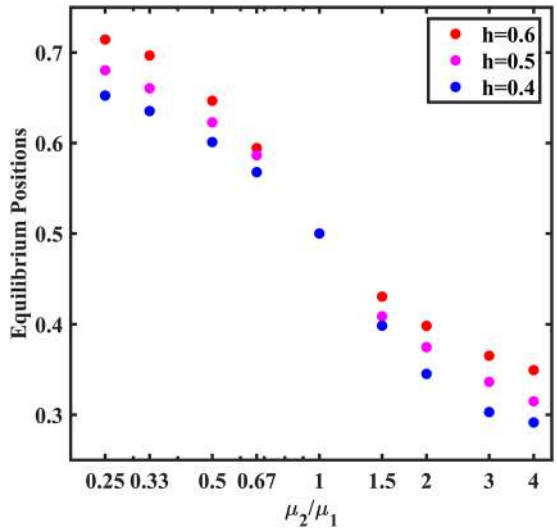

FIG. 9. Effect of the viscosity ratio on equilibrium positions for different interface locations (Re = 10, a/H = 0.2).

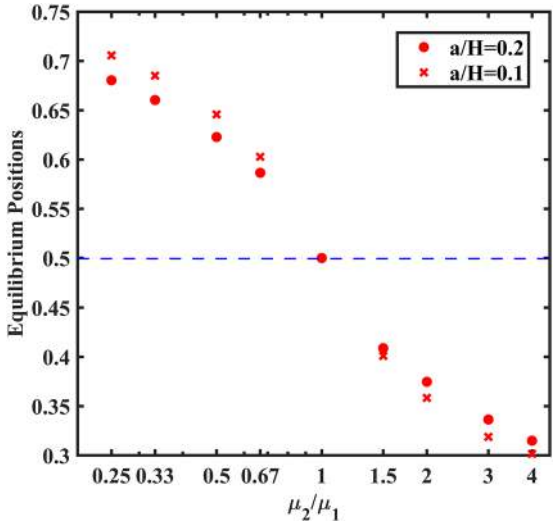

FIG. 10. Effect of the viscosity ratio on equilibrium positions for two particle sizes (Re = 10 and h = 0.5) (blue dashed line: interface).

viscosity ratio of the two fluids. Experimentally, the flow rate of the two liquids determines the pressure drop and the interface position. The velocity profile of stratified flows in 2D and 3D channels can be determined analytically.[27] The interface position and pressure drop of the system used in our simulations are chosen to be consistent with the flow rate ratios and the Reynolds number obtained from the analytical solution.

We present our results in terms of parameters that can be tuned directly such as the flow rate ratio, the viscosity ratio, and the Reynolds number. Here, we discuss how the equilibrium positions change with the viscosity ratio and flow rate ratios of the two liquids. The flow rate ratio of the top fluid to the bottom fluid is

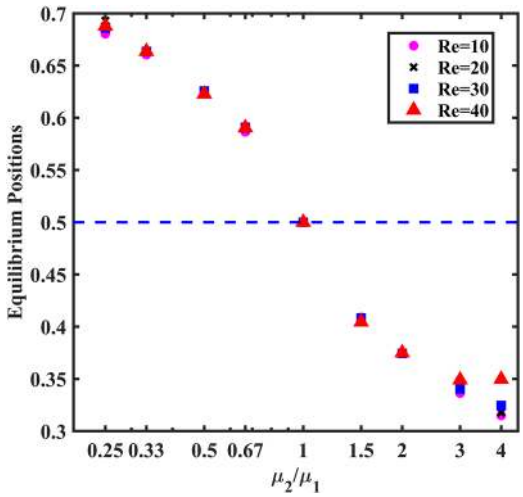

FIG. 11. Effect of the viscosity ratio on equilibrium positions for different Reynolds numbers (a/H = 0.2 and h = 0.5) (blue dashed line: interface).

TABLE I. Equilibrium positions for Re = 10 and Re = 100 for different viscosity ratios.

$\frac{\mu_2}{\mu_1}$	Equilibrium position for Re = 10	Equilibrium position for Re = 100
0.25	0.680	0.691
0.33	0.660	0.671
0.5	0.623	0.636
0.67	0.586	0.61

defined as $q_r = (\frac{q_2}{q_1})$. In all simulations, the viscosity of the top fluid is fixed as 0.2 in lattice units, while the viscosity of the bottom fluid is varied to change the viscosity ratio. We construct the lift force curve and find the locations where the lift force becomes zero to find the equilibrium positions. Figures 12(a) and 12(b) show the lift force curves for two different viscosity ratios, 0.5 and 2 when $q_r = 1$. The lift curve of stratified flows is skewed unlike the lift curve obtained for single phase systems. We observe that when we introduce viscosity stratification, the symmetry of the system is broken and hence we obtain asymmetric stable equilibrium positions. These equilibrium positions are determined by the viscosity ratio and the flow rate ratio q_r. For the current analysis, we examine how they are affected by the viscosity ratio of the system for three different flow rate ratio values.

Figures 13(a)–13(c) show the effect of the viscosity ratio on the equilibrium positions for different q_r when Re = 10. As the viscosity of the bottom fluid is decreased (i.e., as the viscosity ratio is increased), all the equilibrium positions, both stable and unstable, move toward the bottom fluid for all values of q_r. We again denote the stable equilibrium positions as S1 and S2. The top fluid is assumed as a carrier fluid, which contains particles, and we determine conditions when the particles get transferred to the bottom fluid, which is the receiver fluid. The final position of a particle depends on its initial position, as explained in Sec. IV B. We observe that for all cases, S1 lies in the bottom fluid. If both S2 and S1 lie in the bottom fluid, this would imply that the final focusing position would be in the bottom fluid irrespective of the position in which the particle enters the system. Hence, we are interested in the location of S2 and the unstable equilibrium position as q_r is decreased, as these decide in which fluid the particles would finally focus. Specifically, we want to determine the critical viscosity ratio above which all focusing positions are in the bottom fluid for a given q_r.

For the case when $q_r = 1$, both S2 and the unstable equilibrium position lie in the top fluid for the range of viscosity ratios from 0.25 to 1, as shown in Fig. 13(a). For this range of viscosity ratios, if the initial position of the particle is between the unstable position and the interface, the particle would migrate to the bottom fluid and focus at S1. If the particle enters above the unstable position, the particle would focus at S2 and remain in the top fluid. For this combination of q_r and viscosity ratio, some particles may move to the bottom fluid, while some remain in the top fluid depending on their initial positions. So, we are not guaranteed perfect transfer of particles from the top fluid to the bottom fluid. For $q_r = 1$, when the viscosity ratio is more than unity (i.e., when the bottom fluid has a lower viscosity), the unstable position lies in the bottom fluid and S2

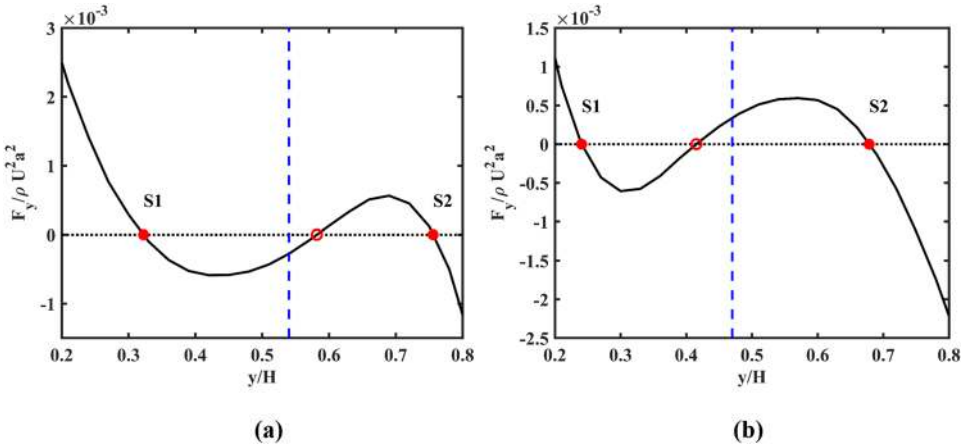

FIG. 12. Lift force curves for stratified pressure driven flows (Re = 10, a/H = 0.2, q_r = 1): (a) μ_2/μ_1 = 0.5 and (b) μ_2/μ_1 = 2. The equilibrium positions obtained are (0.32, 0.58, 0.75) and (0.24, 0.41, 0.67), respectively. (Red filled circle: stable equilibrium position, red hollow circle: unstable equilibrium position, blue dashed line: interface position).

lies in the top fluid. Hence, for this range of viscosity ratios, none of the particles migrate to the bottom fluid.

In Fig. 13(b), the unstable position lies in the bottom fluid for all viscosity ratios when q_r is 0.5. For all viscosity ratios below 4, S2 lies in the top fluid, which implies that the particles entering the top fluid would continue to remain in the top fluid at equilibrium. S2 crosses the interface from the top fluid to the bottom beyond a viscosity ratio value of 4. Since both the stable equilibrium positions lie in the bottom fluid for this ratio, all the particles entering the channel would focus in the bottom fluid. When q_r is decreased to 0.33, the crossover of S2 across the interface occurs when the viscosity ratio is 2 [Fig. 13(c)]. This implies that for all viscosity ratios above 2, migration of particles from the top fluid to the bottom fluid is guaranteed.

When we have a stratified flow of two fluids with one of them carrying particles, we see that there can be no transfer, imperfect transfer, or complete transfer of particles depending on the flow rate ratio (q_r) and the viscosity ratio. When q_r is unity, we achieve an imperfect transfer of particles, while when q_r is 0.5 or 0.33 complete particle transfer occurs after a certain viscosity ratio.

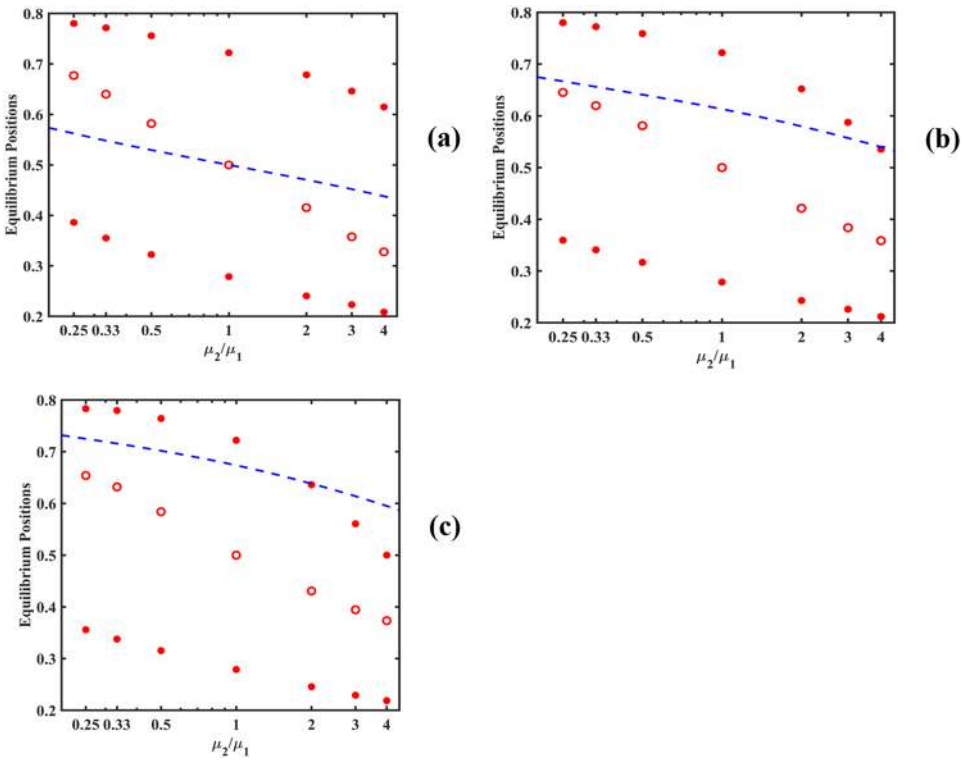

FIG. 13. Effect of the viscosity ratio on the equilibrium positions for (a) q_r = 1, (b) q_r = 0.5, and (c) q_r = 0.33 (Re = 10, a/H = 0.2) (red filled circle: stable equilibrium positions, red hollow circle: unstable equilibrium positions, blue dashed line: interface position).

This analysis shows that decreasing q_r decreases the limiting viscosity ratio above which the crossover of particles is guaranteed. Physically, this implies that for this to occur, q_r must be less than 1, i.e., the bottom fluid or the receiving fluid must have a higher flow rate than the top fluid, which is the carrier fluid. This implies that physically the viscosity of the receiving fluid must be lower than the carrier fluid, as we observe that the crossover occurs when the viscosity ratio is more than one. Our analysis shows that by manipulating q_r for a specific viscosity ratio of the two fluids, we can achieve complete crossover of particles from the carrier fluid to the receiving fluid. This has practical implications in developing membraneless devices for the transfer of particles or cells from one fluid to another.

C. 3D stratified pressure driven flow

To understand the effect of confinement in rectangular microchannels, we extend our analysis by performing 3D simulations of stratified pressure driven flows. The viscosity of the top fluid is fixed as 0.1 in lattice units, and the viscosity of the bottom fluid is varied to change the viscosity ratio. The flow rate ratio is defined as $q_r = (\frac{q_2}{q_1})$, and the aspect ratio is set as unity. To determine focusing positions, we obtain force profiles as reported by Prohm and Stark.[6] The plots are obtained following the methodology of the lift force curves of 2D flows. The particle motion in the x and y directions is restricted, and the forces in the lateral direction acting on the particle at steady state are determined at different locations across the cross section of the channel. These forces are then interpolated to obtain the possible trajectories a free particle would follow, and the equilibrium positions are found where the force vanishes. As the channel is 3D, we encounter saddle positions along with stable equilibrium positions. We would have two stable equilibrium positions in each case. As in the case of the 2D Poiseuille flow, we assume that the top fluid is a carrier fluid containing particles, while the bottom fluid is the receiver fluid. One of the stable equilibrium points always lies in the bottom fluid. We obtain a complete transfer of particles when both the stable equilibrium points lie below the interface separating the two liquids. Invoking the symmetry of the system about the y axis, the force profiles are simulated for only one half of the channel to reduce the computational effort.

Figure 14 shows how the stable equilibrium positions (depicted as green filled squares) change for varying values of μ_2/μ_1 for $q_r = 0.33$ and Re = 10. For the viscosity ratio of 1.5, the upper stable equilibrium position lies above the interface, which implies that all particles entering the system in the top fluid may not get transferred to the bottom fluid. But when the viscosity ratio is increased to 2, the upper stable equilibrium position and the interface move closer to each other. When the viscosity ratio is further increased to 3, both the stable equilibrium positions lie in the bottom fluid, which implies that all the particles entering in the top fluid would get focused in the bottom fluid. It would mean that for the considered combination of q_r and the Reynolds number, a viscosity ratio around 2 is the critical viscosity ratio above which particle transfer is ensured. This is consistent with the conclusion drawn from 2D pressure driven flows where we saw that for a fixed q_r there exists a limiting viscosity ratio above which particle migration is guaranteed from the top fluid to the bottom fluid.

We can see a similar trend when the viscosity ratio is fixed and q_r is decreased. Figure 15 shows how the stable equilibrium positions change by varying values of q_r for $\mu_2/\mu_1 = 3$ and Re = 10. For $q_r = 1$, the upper stable equilibrium position lies in the top fluid. When q_r is set to 0.5, the upper stable equilibrium position and the interface move closer to each other. However, the upper stable equilibrium position continues to remain in the top fluid. It crosses the interface and moves to the bottom fluid when q_r is 0.33. In this case, since both the stable equilibrium positions lie in the bottom fluid, we are guaranteed that the particles in the top fluid would cross the interface and focus in the bottom fluid. For a fixed viscosity ratio, particle

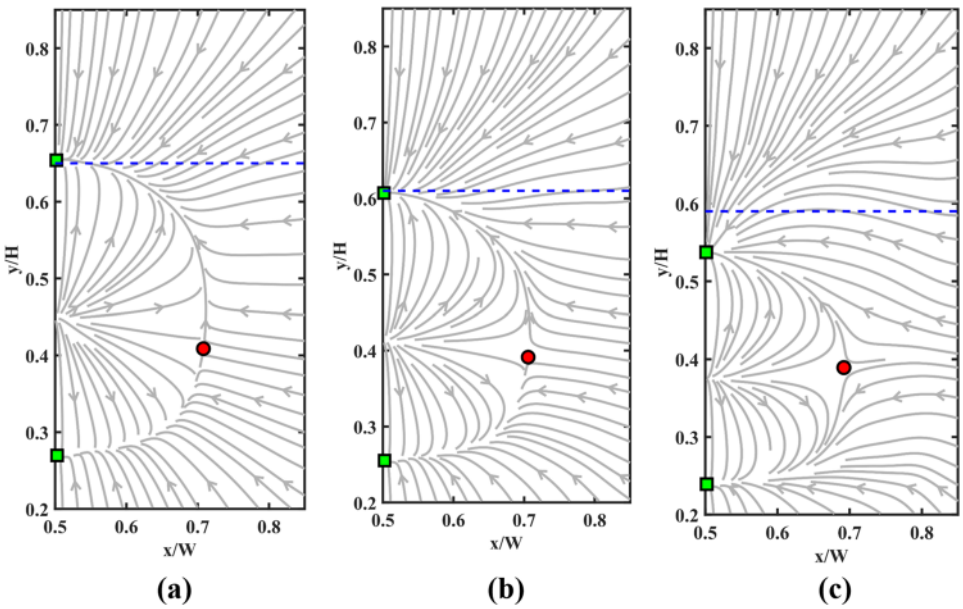

FIG. 14. Force profiles of 3D Poiseuille flows showing the effect of the viscosity ratio on the stable equilibrium positions for (a) $\mu_2/\mu_1 = 1.5$, (b) $\mu_2/\mu_1 = 2$, and (c) $\mu_2/\mu_1 = 3$ (Re = 10, $q_r = 0.33$, a/H = 0.2) (green squares: stable equilibrium position, red circle: saddle equilibrium position, blue dashed line: interface position, gray curves: trajectories followed by the particle).

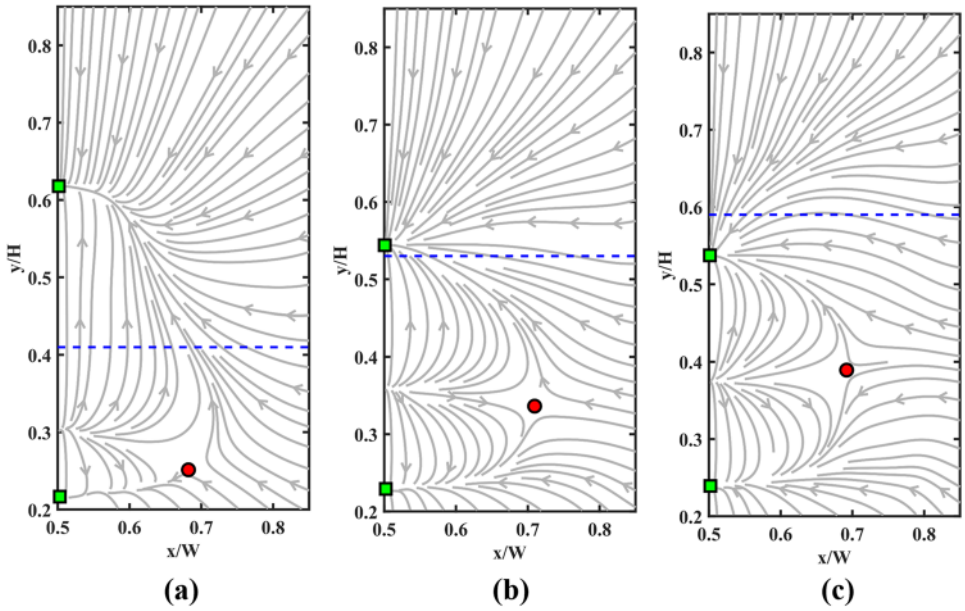

FIG. 15. Force profiles of 3D Poiseuille flows showing the effect of the flow rate on the stable equilibrium positions for (a) q_r = 1, (b) q_r = 0.5, and (c) q_r = 0.33 (Re = 10, μ_2/μ_1 = 3, a/H = 0.2) (green squares: stable equilibrium position, red circle: saddle equilibrium position, blue dashed line: interface position, gray curves: trajectories followed by the particle).

migration across the fluids occurs when q_r is decreased, i.e., when the flow rate of the bottom or the receiving fluid is increased. Hence, a flow rate of the bottom fluid or the receiving fluid greater than a threshold value is necessary for particle transfer. This again is consistent with the results obtained from our analysis of 2D pressure driven stratified flows.

VI. CONCLUSIONS

Particle focusing in stratified Couette and pressure driven flows is analyzed theoretically using a numerical method. 2D and 3D simulations are performed by employing an IB-LBM algorithm. For Couette flows, it is found that the particle would focus on the lower viscosity fluid when the interface is at the center and that the Reynolds number of the system does not affect the focusing positions. It is also found that smaller particles move toward the nearer wall. For stratified pressure driven flows, the presence of a limiting viscosity over which particle transfer occurs toward the lower viscosity fluid is established. The limiting viscosity ratio is found to decrease as the flow rate of the lower viscosity fluid is increased, i.e., when the flow rate ratio is decreased. Force profiles are constructed to determine equilibrium positions in 3D flows.

In this work, we assumed the fluid to be single phase with a sharp viscosity stratification. Despite this assumption of no interfacial forces, the developed model was able to describe how particle focusing would depend qualitatively on experimentally tunable parameters such as the flow rate ratio, viscosity ratio, and Reynolds number. Future work in this area could also include the interfacial forces by employing a multiphase model.

APPENDIX: SCALING AND BOUNDARY CONDITIONS EMPLOYED IN THE LATTICE BOLTZMANN SIMULATIONS

The parameter selection and boundary conditions in LBM are as described in the work of Krüger *et al.*[23]

1. Parameter selection in LBM

The lattice parameters are related to the physical parameters using conversion factors. The conversion factors for the grid size, time step, and density are obtained as

$$C_x = \frac{\Delta x_p}{\Delta x_{lbm}}, \tag{A1}$$

$$C_t = \frac{\Delta t_p}{\Delta t_{lbm}}, \tag{A2}$$

$$C_\rho = \frac{\rho_p}{\rho_{lbm}}. \tag{A3}$$

Here, the quantities with the subscript p indicate the physical parameter values and the quantities with the subscript lbm represent the lattice parameters. We keep Δx_{lbm}, Δt_{lbm}, and ρ_{lbm} equal to unity. Hence, these conversion factors would be equal to the physical values of the grid size, time step, and density. Therefore, N_x grids along a direction span a length of $N_x{}^* \Delta x_{lbm}$ in lattice scale, and since Δx_{lbm} = 1, N_x represents the length in lattice units.

C_x, C_t, and C_ρ form a basis from which conversion factors of other physical quantities are obtained using a dimensional analysis. For example, the conversion factor of the force is related to the basic conversion factors as $C_f = C_\rho C_x{}^4/C_t{}^2$ and the conversion factor for the kinematic viscosity would be $C_\vartheta = C_x{}^2/C_t$.

When a system is simulated and described only using nondimensional parameters, it is sufficient to make sure that the combination of the lattice parameters also produces the same nondimensional parameter values. For example, if we are simulating a system with a given Reynolds number, it is sufficient to ensure that the Reynolds number is related to the lattice parameters as

$Re_{lbm} = \frac{H_{lbm}U_{lbm}}{\vartheta_{lbm}}$. This results in

$$Re_{lbm} = \frac{H_{lbm}U_{lbm}}{\vartheta_{lbm}} = \frac{H_p * U_p * C_\vartheta}{C_x * C_u * \vartheta_p} = \frac{H_p U_p}{\vartheta_p} * \frac{C_\vartheta}{\frac{C_x^2}{C_t}} = \frac{H_p U_p}{\vartheta_p} = Re_p. \tag{A4}$$

Defining the Reynolds numbers in terms of the lattice parameter is equivalent to defining a physical system with the same Reynolds number. This is to be true for all nondimensional parameters. Hence, the simulation parameters in LBM space are chosen so that the combination of parameters matches with the set nondimensional number.

2. Boundary conditions in LBM

Here, we describe the boundary conditions used in 2D simulations for the D2Q9 velocity set. The particle density functions f_i at the boundary that has a velocity component transverse to it would be unknown. For example, the values of f_4, f_7, and f_8 would be unknown in the top boundary, and the values of f_2, f_5, and f_6 would be unknown in the bottom boundary. Special rules like the bounce back condition or the wet node condition are employed to find them.

a. Bounce back condition

The bounce back condition assumes the simulation boundary to be at a half grid distance away from the physical wall. Here, the unknown particle density function values are found using the relation

$$f_i(x_b, t + \Delta t) = f_i^*(x_b, t) - 2w_i\rho_w \frac{\boldsymbol{c_i} \cdot \boldsymbol{u_w}}{{c_s}^2}, \tag{A5}$$

where ρ_w and u_w are the density and the velocity at the wall, respectively. f_i indicates the density function associated with the velocity opposite to that of f_i, i.e., $\boldsymbol{c_i} = -\boldsymbol{c_i}$. The unknown f_i at the top boundary are obtained as

$$\begin{aligned} f_4(x_b, t + \Delta t) &= f_2^*(x_b, t) - 2w_2\rho_w \frac{u_{wy}}{{c_s}^2}, \\ f_7(x_b, t + \Delta t) &= f_5^*(x_b, t) - 2w_5\rho_w \frac{(u_{wx} + u_{wy})}{{c_s}^2}, \\ f_8(x_b, t + \Delta t) &= f_6^*(x_b, t) - 2w_6\rho_w \frac{(-u_{wx} + u_{wy})}{{c_s}^2}. \end{aligned} \tag{A6}$$

The unknown f_i at the bottom boundary are obtained as

$$\begin{aligned} f_2(x_b, t + \Delta t) &= f_4^*(x_b, t) + 2w_4\rho_w \frac{u_{wy}}{{c_s}^2}, \\ f_5(x_b, t + \Delta t) &= f_7^*(x_b, t) + 2w_7\rho_w \frac{(u_{wx} + u_{wy})}{{c_s}^2}, \\ f_6(x_b, t + \Delta t) &= f_8^*(x_b, t) + 2w_8\rho_w \frac{(-u_{wx} + u_{wy})}{{c_s}^2}. \end{aligned} \tag{A7}$$

b. Wet node boundary condition

The wet node boundary condition assumes the simulation boundary to be exactly at the physical wall unlike the bounce back condition. Here, the unknown populations are found using two steps—(a) the unknown density at the wall ρ_w is found using the set wall velocity u_w and known particle density functions, f_i, and (b) unknown f_i are found from the known f_i and ρ_w. At the top boundary, the following steps are carried out:

$$\rho_w = \frac{1}{1 + u_{wy}}[f_0 + f_1 + f_3 + 2(f_2 + f_5 + f_6)], \tag{A8}$$

$$\begin{aligned} f_4 &= f_2 - \frac{2}{3}\rho_w u_{wy}, \\ f_7 &= f_5 + \frac{1}{2}(f_1 - f_3) - \frac{1}{2}\rho_w u_{wx} - \frac{1}{6}\rho_w u_{wy}, \\ f_8 &= f_6 - \frac{1}{2}(f_1 - f_3) + \frac{1}{2}\rho_w u_{wx} - \frac{1}{6}\rho_w u_{wy}. \end{aligned} \tag{A9}$$

Also, at the bottom boundary, we implement

$$\rho_w = \frac{1}{1 - u_{wy}}[f_0 + f_1 + f_3 + 2(f_4 + f_7 + f_8)], \tag{A10}$$

$$\begin{aligned} f_2 &= f_4 + \frac{2}{3}\rho_w u_{wy}, \\ f_5 &= f_7 - \frac{1}{2}(f_1 - f_3) + \frac{1}{2}\rho_w u_{wx} + \frac{1}{6}\rho_w u_{wy}, \\ f_6 &= f_8 + \frac{1}{2}(f_1 - f_3) - \frac{1}{2}\rho_w u_{wx} + \frac{1}{6}\rho_w u_{wy}. \end{aligned} \tag{A11}$$

Here, u_{wx} and u_{wy} are the x component and the y component of the velocity at the wall and all f_i represents the particle density function values at the boundary.

REFERENCES

[1] G. Segré and A. Silberberg, "Behaviour of macroscopic rigid spheres in Poiseuille flow. Part 2. Experimental results and interpretation," J. Fluid Mech. **14**, 136 (1962).

[2] J. M. Martel and M. Toner, "Inertial focusing in microfluidics," Annu. Rev. Biomed. Eng. **16**, 371 (2014).

[3] J. Seo, M. H. Lean, and A. Kole, "Membrane-free microfiltration by asymmetric inertial migration," Appl. Phys. Lett. **91**, 033901 (2007).

[4] A. J. Mach and D. di Carlo, "Continuous scalable blood filtration device using inertial microfluidics," Biotechnol. Bioeng. **107**, 302 (2010).

[5] D. Di Carlo, J. F. Edd, K. J. Humphry, H. A. Stone, and M. Toner, "Particle segregation and dynamics in confined flows," Phys. Rev. Lett. **102**, 094503 (2009).

[6] C. Prohm and H. Stark, "Feedback control of inertial microfluidics using axial control forces," Lab Chip **14**, 2115 (2014).

[7] K. Miura, T. Itano, and M. Sugihara-Seki, "Inertial migration of neutrally buoyant spheres in a pressure-driven flow through square channels," J. Fluid Mech. **749**, 320 (2014).

[8] N. Nakagawa, T. Yabu, R. Otomo, A. Kase, M. Makino, T. Itano, and M. Sugihara-Seki, "Inertial migration of a spherical particle in laminar square channel flows from low to high Reynolds numbers," J. Fluid Mech. **779**, 776 (2015).

[9] B. Chun and A. J. C. Ladd, "Inertial migration of neutrally buoyant particles in a square duct: An investigation of multiple equilibrium positions," Phys. Fluids **18**, 031704 (2006).

[10] A. A. S. Bhagat, S. S. Kuntaegowdanahalli, and I. Papautsky, "Inertial microfluidics for continuous particle filtration and extraction," Microfluid. Nanofluid. **7**, 217 (2009).

[11] J. Feng, H. H. Hu, and D. D. Joseph, "Direct simulation of initial value problems for the motion of solid bodies in a Newtonian fluid. Part 2. Couette and Poiseuille flows," J. Fluid Mech. **277**, 271 (1994).

[12]A. Shamloo and A. Mashhadian, "Inertial particle focusing in serpentine channels on a centrifugal platform," Phys. Fluids **30**, 012002 (2018).
[13]T. Inamuro, K. Maeba, and F. Ogino, "Flow between parallel walls containing the lines of neutrally buoyant circular cylinders," Int. J. Multiphase Flow **26**, 1981 (2000).
[14]R. Verberg and A. Ladd, "Lattice-Boltzmann simulations of particle-fluid suspensions," J. Stat. Phys. **104**, 1191 (2001).
[15]W. Liu and C.-Y. Wu, "Analysis of inertial migration of neutrally buoyant particle suspensions in a planar Poiseuille flow with a coupled lattice Boltzmann method-discrete element method," Phys. Fluids **31**, 063301 (2019).
[16]J. Hu and Z. Guo, "A numerical study on the migration of a neutrally buoyant particle in a Poiseuille flow with thermal convection," Int. J. Heat Mass Transfer **108**, 2158 (2017).
[17]Z. G. Feng and E. E. Michaelides, "The immersed boundary-lattice Boltzmann method for solving fluid-particles interaction problems," J. Comput. Phys. **195**, 602 (2004).
[18]J. Wu and C. Shu, "Implicit velocity correction-based immersed boundary-lattice Boltzmann method and its applications," J. Comput. Phys. **228**, 1963 (2009).
[19]K. Suzuki and T. Inamuro, "Effect of internal mass in the simulation of a moving body by the immersed boundary method," Comput. Fluids **49**, 173 (2011).
[20]D. Lee, S. M. Nam, J. A. Kim, D. Di Carlo, and W. Lee, "Active control of inertial focusing positions and particle separations enabled by velocity profile tuning with coflow systems," Anal. Chem. **90**, 2902 (2018).
[21]D. R. Gossett, H. T. K. Tse, J. S. Dudani, K. Goda, T. A. Woods, S. W. Graves, and D. Di Carlo, "Inertial manipulation and transfer of microparticles across laminar fluid streams," Small **8**, 2757 (2012).
[22]J. O'Connor, P. Day, P. Mandal, and A. Revell, "Computational fluid dynamics in the microcirculation and microfluidics: What role can the lattice Boltzmann method play?," Integr. Biol. **8**, 589 (2016).
[23]T. Krüger, H. Kusumaatmaja, A. Kuzmin, O. Shardt, G. Silva, and E. M. Viggen, *The Lattice Bolyzmannn Method: Principles and Practice* (Springer, Switzerland, 2017).
[24]C. S. Peskin, "The immersed boundary method," Acta Numer. **11**, 479 (2002).
[25]T. Kruger, in LBM Workshop, 2011.
[26]Z. G. Feng and E. E. Michaelides, "Robust treatment of no-slip boundary condition and velocity updating for the lattice-Boltzmann simulation of particulate flows," Comput. Fluids **38**, 370 (2009).
[27]A. B. Vir, S. R. Kulkarni, J. R. Picardo, A. Sahu, and S. Pushpavanam, "Holdup characteristics of two-phase parallel microflows," Microfluid. Nanofluid. **16**, 1057 (2014).